Available online at www.sciencedirect.com
SCIENCE DIRECT®
International Journal of Heat and Mass Transfer 47 (2004) 1159–1174
International Journal of HEAT and MASS TRANSFER
www.elsevier.com/locate/ijhmt

Comparison of volumetric and surface heating sources in the modeling of laser melting of ceramic materials

J.F. Li [a,b,*], L. Li [a], F.H. Stott [b]

[a] Laser Processing Research Centre, Department of Mechanical, Aerospace and Manufacturing Engineering, University of Manchester Institute of Science and Technology (UMIST), P.O. Box 88, Manchester M60 1QD, UK
[b] Corrosion and Protection Centre, UMIST, P.O. Box 88, Manchester M60 1QD, UK

Received 15 November 2002; received in revised form 3 October 2003

Abstract

It is known that laser beam absorption length for ceramic materials is several orders of magnitude larger than that of metallic materials. Therefore the use of surface heating source in the modeling of laser melting of ceramics may not be correct. In this paper, thermal fields have been modeled with both a volumetric heating source and a surface heating source to predict the melt cross-sections of an Al_2O_3-based refractory during CO_2 laser treatment. Three-dimension quasi-steady state heat conduction equations are solved by applying the Green function method, while the singularities associated with the numerical integration are dealt with using a linear interpolation method. It has been experimentally confirmed that the model incorporating the volumetric heating source is more accurate than that incorporating the surface heating source. The melt depths and widths predicted from the model using the volumetric heating source are in excellent agreement with the experimental data. The predicted cross-sectional profiles of the melt/solid interfaces are also consistent with the experimental results for smaller melt cross-sections. However, increasing discrepancy has been observed with the increase in size of the melt cross-section.

Keywords: Laser; Melting; Ceramics; Modeling; Numerical integration

1. Introduction

Laser surface treatment of ceramic materials, such as architecture and refractory materials, has drawn increased interest over recent years [1–5]. In particular, sealing alumina-based refractory surfaces by laser melting has been shown to be a practical approach to preparing high performance refractory materials that retain the bulk material properties while improving the surface properties of conventional materials [4,5]. A key aspect during such laser surface processing is to avoid the occurrence of cracks due to thermal-induced stresses. Various methods have been employed to overcome this problem; such experimental investigations have shown possibility of achieving crack-free and dense laser-treated surface layers for industrial applications [4–7].

On the other hand, theoretical models could offer cost-effective and highly flexible means for analysing and optimizing laser surface processing. In order to avoid the occurrence of cracks during laser melting of ceramic materials, it is essential to understand and control the laser-induced thermal field, i.e. the temperature distribution in the treated materials. The physical processes that take place during laser surface melting include heat transfer into the material, radiative and convective boundary conditions, thermo-dynamics of phase-changes, a moving boundary at the melt/solid interface, fluid flow, surface tension and mass transportation within the

* Corresponding author. Address: Laser Processing Research Centre, Department of Mechanical, Aerospace and Manufacturing Engineering, University of Manchester Institute of Science and Technology (UMIST), P.O. Box 88, Manchester M60 1QD, UK. Tel.: +44-161-200-3827; fax: +44-161-200-3803.
E-mail address: j.li-3@umist.ac.uk (J.F. Li).

0017-9310/$ - see front matter © 2003 Elsevier Ltd. All rights reserved.
doi:10.1016/j.ijheatmasstransfer.2003.10.002

Nomenclature

a	characteristic laser beam radius [m]
d	laser beam diameter [m]
c	specific heat [$J\,kg^{-1}\,K^{-1}$]
D	melt depth [m]
f	fraction of laser mode structure that contains the Gaussian mode
G	Green function
I	laser intensity as surface heating source [$W\,m^{-2}$]
k	thermal conductivity [$W\,m^{-1}\,K^{-1}$]
P	total power of laser beam [W]
Pe	Péclet number
P_V	rate of heat loss due to vaporization [W]
q	laser intensity as volumetric heating source [$W\,m^{-3}$]
R	reflectivity of workpiece material
S	melt cross-sectional area [m^2]
S_b	cross-sectional area of vapour phase [m^2]
T	absolute temperature [K]
T_0	environmental temperature [K]
T_b	boiling point of workpiece material [K]
T_m	melting point of workpiece material [K]
U	workpiece moving velocity [$m\,s^{-1}$]
u, v, w	x, y and z components of velocity [$m\,s^{-1}$]
W	melt half-width [m]
x, y, z	Cartesian coordinates [m]
X', Y', Z'	dimensionless Cartesian coordinates
z_{cs}	cross-sectional profile of melt/solid interface [m]
z_{mp}	melt/solid interface [m]
z_{vp}	vapour/melt interface [m]
z_{vpcs}	cross-sectional profile of vapour/melt interface [m]

Greek symbols

α	thermal diffusivity [$m^2\,s^{-1}$]
β	power that is used to describe approximately the melt cross-sectional profile
γ	laser absorption length of workpiece material [m]
ρ	density of workpiece material [$kg\,m^{-3}$]
σ_T	temperature coefficient of surface tension [$N\,m^{-1}\,K^{-1}$]
τ_{xz}	moment flux along z direction due to x component of velocity [$N\,m^{-2}$]
τ_{yz}	moment flux along z direction due to y component of velocity [$N\,m^{-2}$]

Superscripts

$'$	dimensionless quantity
i, j, k	serial number of the Gaussian–Legendre integral points

Subscripts

E	experimental value
P	predicted value
ref	reference quantity
S	value predicted from the model using a surface heating source
V	value predicted from the model using a volumetric heating source

molten body [8,9]. An exact theoretical model for analysing the thermal field is thus extremely complicated and requires numerical approaches, e.g., finite difference method or finite element method. However, such numerical approaches still need considerable computer power and long computing time [10]. Therefore, it is necessary to have simpler analytical models to predict rapidly the effect of process parameters and to provide the basis for more complicated computational models [11,12].

In order to determine the temperature profiles and/or geometry parameters of treated tracks during laser melting, many analytical models have been developed to explain and predict the effects of laser-induced heating and melting of materials [11–17]. Comprehensive reviews of such mathematical models have been given in [17,18]. These models are mainly based on the classic analytical solution derived by Carslaw and Jeager in terms of integrals over the surface of the expression for a point source [13]. These were predominately focused on laser melting of metallic materials. In addition, in order to achieve satisfactory results, a continuous Gaussian mode for the laser beam, carefully selected laser process parameters or semi-empirical approaches were usually employed.

Theoretically, most ceramic materials are poor absorbers of heat and much less reflective than metals to long infrared laser wavelengths; hence, CO_2 laser energy tends to penetrate more effectively such materials than metals [19]. Lawrence et al. [20,21] experimentally confirmed the absorption lengths of a CO_2 laser for a concrete and a high-volume Al_2O_3-based refractory to be 470 ± 22 μm and 345 ± 22 μm respectively as compared to less than 0.1 μm for most metallic materials. The laser-induced thermal fields for ceramics should thus be more appropriately modeled with volumetric heating sources. However, surface heating sources by which thermal fields were modeled, have been widely used in investigations of laser surface treatments of ceramic materials [17,22].

Although some thermal models that incorporate volumetric heating sources with stationary or moving Gaussian laser sources have been developed [15,16], analytical models for laser surface melting that incorporate a moving steady volumetric heating source and applicable to any spatial mode of laser beam has not been found in the existing literature. In the present work, the thermal field in a type of high-volume alumina-based refractory during CO_2 laser surface melting has been modeled with a volumetric heating source, while also with a surface heating source for comparison purposes. In the calculation cases, a mixed mode of Gaussian beam and Doughnut beam was chosen, but particular efforts were made to assure that the models can incorporate any beam intensity distributions. The main purpose of the present modeling was to predict rapidly the melt cross-sections of ceramic materials and to build a basis for more complicated computational models to determine the temperature and stress profiles. Experiments involving laser surface melting of the refractory were also carried out using various laser process parameters, and the measured melt cross-section parameters, including melt depths, widths, areas and cross-section profiles were used to evaluate the validity of the models.

2. Modeling of laser surface melting

2.1. Thermal model description

The laser surface melting of the high-volume alumina-based refractory is briefly illustrated in Fig. 1. A continuous CO_2 laser with sufficient intensity is incident upon a workpiece of the refractory block, moving at a constant velocity. A fraction of the incident light energy is absorbed by the workpiece, and the very intensive heat flux under the laser beam leads to the formation of a melt pool. This then solidifies to produce a dense treated track. This is a typical problem incorporating moving a heating source and phase changes. The aim of the present work has mainly been to develop relatively simple models applicable to any spatial mode of the laser beam to predict the melt cross-sections. The physical assumptions for the model are listed as follows:

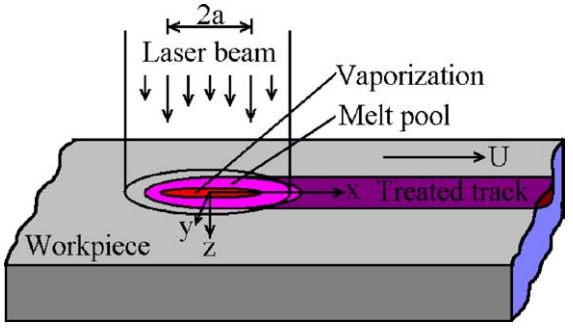

Fig. 1. Schematic diagram of the workpiece during laser surface melting.

(i) The model only considers the quasi-steady heat conduction problem. The initial thermal history of the workpiece material and the effects of fluid flow and mass transportation within the melt pool on heat transfer are neglected, as in a number of previous analytical models [9,11–13,17].

(ii) The workpiece is taken as a semi-infinite body and the surface of the workpiece is adiabatic. This assumption results from the fact that the laser beam size is very small relative to the workpiece and the heat losses by convection and radiation are negligible compared to heat conduction within the workpiece [11,17].

(iii) Latent heat of fusion is not taken into account. The major difficulty in considering latent heat of fusion is associated with a moving phase-change interface, across which certain jump conditions must be satisfied and whose location is unknown a priori [23]. In the numerical modeling, a standard approach for dealing with such phase-change processes is the so-called "fixed-grid enthalpy-based" method [24]. In this method, an appropriate formulation of latent heat function plays a pivotal role in assuring the results from the energy equation consistent with the phase-change consideration. Recently, Chakraborty and Dutta [24] developed a generalized formulation for evaluation of latent heat functions for any phase-change situation. In the present work, a relatively simple model was developed to build a basis for more complicated numerical models to determine the temperature and stress fields. Therefore, the latent heat of fusion was omitted for simplification. This approximation can be quite reasonable because the latent heat absorbed at the melting interface is less than 10% of the incident laser energy and is liberated at the solidifying interface [14].

(iv) Heat loss due to vaporization is taken into consideration since the chosen workpiece material in this work, the refractory brick, is porous, and a sufficiently intensive laser power is needed for the molten body to flow and seal the surface completely. In such a case, vaporization occurs and takes away a considerable amount of heat. However, in order to simplify the calculation procedure, it is assumed that the produced vapour remains in its original place as a liquid phase and the heat taken away by the vaporization is equal to the latent heat of vaporization absorbed by the vapour, which is determined by an iteration method, as detailed in the next sections.

(v) The properties of the refractory brick, such as thermal conductivity, thermal diffusivity and reflectivity, are isotropic and independent of temperature. The property parameters of all solid, liquid and vapour

phases of the workpiece material are identical in value. The porosity of the refractory brick is considered to contribute to reducing thermal conductivity and thermal diffusivity.

(vi) The heating source can be any spatial mode of the laser beam. In the calculations, a mixture of the Gaussian and Doughnut modes is adopted as the volumetric heating source and the surface heating source. For the volumetric source, the laser energy penetrating into the workpiece is expressed by means of the Beer Lambert's law [19–21].

2.2. Mathematical formulation

For mathematical formulation, a Cartesian geometry is employed; the x–y plane of the coordinate system lies on the surface of the workpiece and the origin coincides with the centre of the laser beam (see Fig. 1). The workpiece moves in the positive x direction with a constant velocity U. For a laser beam with intensity distribution of $I(x,y)$, if the workpiece material has an absorption length, γ, to the laser, according to the Beer Lambert's law [19], a volumetric heating source can be expressed as

$$q(x,y,z) = \frac{(1-R)I(x,y)}{\gamma}\exp\left(-\frac{z}{\gamma}\right) \quad -\infty < x < +\infty;\ -\infty < y < +\infty;\ z \geqslant 0 \tag{1}$$

The governing equation of the quasi-steady heat conduction problem is thus given by

$$\nabla^2 T + \frac{U}{\alpha}\frac{\partial T}{\partial x} + \frac{q(x,y,z)}{k} = 0 \quad -\infty < x < +\infty;\ -\infty < y < +\infty;\ z > 0 \tag{2}$$

with the boundary conditions

$$T(x,y,z) = T_0 \quad \text{as } x \to \pm\infty;\quad y \to \pm\infty \tag{3}$$

and

$$k\frac{\partial T(x,y,0)}{\partial z} = -q(x,y,0) \tag{4}$$

The above Eqs. (1)–(4) formulate the thermal model using the volumetric heating source completely. Mathematically, this problem can be transformed into the following problem, defined by Eqs. (5)–(7), to solve the temperature field $T(x,y,z)$.

$$q(x,y,z) = \frac{(1-R)I(x,y)}{\gamma}\exp\left(-\frac{|z|}{\gamma}\right) \quad -\infty < x < +\infty;\ -\infty < y < +\infty;\ -\infty < z < +\infty \tag{5}$$

$$\nabla^2 T + \frac{U}{\alpha}\frac{\partial T}{\partial x} + \frac{q(x,y,z)}{k} = 0 \quad -\infty < x < +\infty;\ -\infty < y < +\infty;\ -\infty < z < +\infty \tag{6}$$

$$T(x,y,z) = T_0 \quad \text{as } x \to \pm\infty;\ y \to \pm\infty;\ z \to \pm\infty \tag{7}$$

The Green's function $G(x,y,z;x_1,y_1,z_1)$ satisfies

$$\nabla^2 G + \frac{U}{\alpha}\frac{\partial G}{\partial x} + \frac{\delta(x-x_1)\delta(y-y_1)\delta(z-z_1)}{k} = 0 \quad -\infty < x < +\infty;\ -\infty < y < +\infty;\ -\infty < z < +\infty \tag{8}$$

$$G(x,y,z;x_1,y_1,z_1) = 0 \quad \text{as } x \to \pm\infty;\ y \to \pm\infty;\ z \to \pm\infty \tag{9}$$

is

$$G(x,y,z;x_1,y_1,z_1) = \frac{1}{4\pi k} \times \frac{\exp\left\{\frac{U}{2\alpha}\left[(x-x_1) - \sqrt{(x-x_1)^2+(y-y_1)^2+(z-z_1)^2}\right]\right\}}{\sqrt{(x-x_1)^2+(y-y_1)^2+(z-z_1)^2}} \tag{10}$$

Then, the temperature $T(x,y,z)$ at a point (x,y,z) for the thermal model defined by Eqs. (1)–(4) can be solved from the triple integral (11) through the application of Eqs. (5)–(10).

$$\begin{aligned} T(x,y,z) &= T_0 + \int_{x_1=-\infty}^{\infty}\int_{y_1=-\infty}^{\infty}\int_{z_1=-\infty}^{\infty} q(x_1,y_1,z_1)\times G(x,y,z;x_1,y_1,z_1)\,\mathrm{d}z_1\,\mathrm{d}y_1\,\mathrm{d}x_1 \\ &= T_0 + \frac{1-R}{4\pi k\gamma}\int_{x_1=-\infty}^{\infty}\int_{y_1=-\infty}^{\infty}\int_{z_1=-\infty}^{\infty} I(x_1,y_1) \\ &\quad\times \frac{\exp\left\{\frac{U}{2\alpha}\left[(x-x_1) - \sqrt{(x-x_1)^2+(y-y_1)^2+(z-z_1)^2}\right] - \frac{|z_1|}{\gamma}\right\}}{\sqrt{(x-x_1)^2+(y-y_1)^2+(z-z_1)^2}}\,\mathrm{d}z_1\,\mathrm{d}y_1\,\mathrm{d}x_1 \end{aligned} \tag{11}$$

If the absorption length, γ, is very small, the incident laser can be simplified as a surface heating source, as modelled in a number of contributions to the laser surface treating of metallic materials [11–13]. In the case of a surface heating source, the governing heat conduction equation is

$$\nabla^2 T + \frac{U}{\alpha}\frac{\partial T}{\partial x} = 0$$
$$-\infty < x < +\infty;\ \ -\infty < y < +\infty;\ \ z > 0 \tag{12}$$

The corresponding boundary conditions are

$$T(x,y,z) = T_0 \quad \text{as } x \to \pm\infty;\ \ y \to \pm\infty \tag{13}$$

and

$$k\frac{\partial T(x,y,0)}{\partial z} = -(1-R)I(x,y) \tag{14}$$

Following the work of Carslaw and Jaegar [13] and Dowden [12], the solution to this surface-heating problem is given as a double integral

$$T(x,y,z) = T_0 + \frac{1-R}{2\pi k}\int_{x_1=-\infty}^{\infty}\int_{y_1=-\infty}^{\infty} I(x_1,y_1)\frac{\exp\left\{\frac{U}{2\alpha}\left[(x-x_1)-\sqrt{(x-x_1)^2+(y-y_1)^2+z^2}\right]\right\}}{\sqrt{(x-x_1)^2+(y-y_1)^2+z^2}}\,\mathrm{d}y_1\,\mathrm{d}x_1 \tag{15}$$

Theoretically, thermal models incorporating a volumetric heating source is more appropriate for ceramic materials. However, surface heating sources are widely used in the thermal modelling of laser surface treatment of ceramic materials [17,22]. Thus in the present model, a surface heating source and a volumetric heating source are both employed for comparison purposes.

Based on Eqs. (11) and (15), the cross-sectional profile of the melt/solid interface, $z_{cs}(y)$, can be readily calculated. The melt/solid interface, $z_{mp}(x,y)$, can be solved from Eq. (16)

$$T(x,y,z_{mp}(x,y)) = T_m \tag{16}$$

Then, $z_{cs}(y)$ is the maximum value of $z_{mp}(x,y)$ for different y values as a function of x, i.e.,

$$z_{cs}(y) = \max(z_{mp}(x,y)) \quad -\infty < x < \infty \tag{17}$$

The melt depth is

$$D = \max(z_{cs}(y)) \quad -\infty < y < \infty \tag{18}$$

The melt half-width is

$$W = \min(|y|) \quad \text{as } z_{cs}(y) = 0 \tag{19}$$

The melt cross-section area

$$S = \int z_{cs}(y)\mathrm{d}y \tag{20}$$

In the present calculations, from consideration of the heat loss by vaporization, the energy distribution of a mixed laser mode of the Gaussian beam and Doughnut beam is expressed as [19]

$$I(x,y) = \frac{P - P_V/(1-R)}{\pi a^2}\left[f + (1-f)\left(\frac{x^2+y^2}{a^2}\right)\right] \times \exp\left(-\frac{x^2+y^2}{a^2}\right)$$
$$-\infty < x < +\infty;\ \ -\infty < y < +\infty \tag{21}$$

Substituting Eq. (21) into Eq. (5), one obtains

$$q(x,y,z) = \frac{(1-R)P - P_V}{\pi a^2\gamma}\left[f + (1-f)\left(\frac{x^2+y^2}{a^2}\right)\right] \times \exp\left(-\frac{x^2+y^2}{a^2} - \frac{|z|}{\gamma}\right)$$
$$-\infty < x < +\infty;\ \ -\infty < y < +\infty;\ \ -\infty < z < +\infty \tag{22}$$

If vaporization does not take place, P_V is taken as zero. When vaporization occurs, the quantity of P_V is used to signify the heat loss due to vaporization. According to assumption (iv),

$$P_V = L_V \rho U S_b \tag{23}$$

where S_b is the cross-sectional area of the vapour phase gap, $z_{vpcs}(y)$, which can be obtained from the vapour/liquid interface $z_{vp}(x,y)$ satisfies

$$T(x,y,z_{vp}(x,y)) = T_b \tag{24}$$

Similar to the solution of $z_{cs}(y)$, $z_{vpcs}(y)$ is the maximum value of $z_{vp}(x,y)$ at different y values as a function of x, i.e.,

$$z_{vpcs}(y) = \max(z_{vp}(x,y)) \quad -\infty < x < \infty \tag{25}$$

$$S_b = \int z_{vpcs}(y)\mathrm{d}y \tag{26}$$

When vaporization occurs, the solution derived above cannot be solved directly because the value of P_V is initially unknown. Thus an iterative process is necessary to solve the problem.

If the following dimensionless groups are introduced

$$X' = \frac{x}{a};\quad Y' = \frac{y}{a};\quad Z' = \frac{z}{a};\quad \gamma' = \frac{\gamma}{a};$$
$$T' = \frac{T - T_0}{[(1-R)P - P_V]/(4\pi^2 a\gamma' k)};$$
$$T'_m = \frac{T_m - T_0}{[(1-R)P - P_V]/(4\pi^2 a\gamma' k)};$$
$$T'_b = \frac{T_b - T_0}{[(1-R)P - P_V]/(4\pi^2 a\gamma' k)};\quad Pe = \frac{Ua}{2\alpha} \tag{27}$$

Then, Eqs. (11) and (15) are changed to the dimensionless forms, as (28) and (29), respectively.

$$T'(X',Y',Z') = \int_{X_1'=-\infty}^{\infty}\int_{Y_1'=-\infty}^{\infty}\int_{Z_1'=-\infty}^{\infty}[f+(1-f)(X_1'^2+Y_1'^2)]\exp[-(X_1'^2+Y_1'^2)] \times \frac{\exp\left\{Pe\left[(X'-X_1')-\sqrt{(X'-X_1')^2+(Y'-Y_1')^2+(Z'-Z_1')^2}\right]-\frac{|Z_1'|}{\gamma'}\right\}}{\sqrt{(X'-X_1')^2+(Y'-Y_1')^2+(Z'-Z_1')^2}}\,dZ_1'\,dY_1'\,dX_1' \tag{28}$$

$$T'(X',Y',Z') = 2\gamma'\int_{X_1'=-\infty}^{\infty}\int_{Y_1'=-\infty}^{\infty}[f+(1-f)(X_1'^2+Y_1'^2)]\exp[-(X_1'^2+Y_1'^2)] \times \frac{\exp\left\{Pe\left[(X'-X_1')-\sqrt{(X'-X_1')^2+(Y'-Y_1')^2+(Z'-Z_1')^2}\right]\right\}}{\sqrt{(X'-X_1')^2+(Y'-Y_1')^2+(Z'-Z_1')^2}}\,dY_1'\,dX_1' \tag{29}$$

2.3. Numerical procedures

Double and triple numerical integrations are usually necessary to solve the thermal fields expressed as Eqs. (11) and (15), or the corresponding dimensionless forms, Eqs. (28) and (29). However, these equations can be singular at the numerical integration points, as viewed in the example in Fig. 2. If the incident laser intensity is continuous over the whole integral domain, as is the case for Eqs. (21) and (22), the singularities can be avoided by means of a suitable coordinate transformation. One of the aims of the present modelling is to produce relatively simple models that can incorporate any mode of laser beam. An alternative approach is therefore employed to deal with the singularities associated with the numerical integration.

Knowing that the laser energy distributed in locations outside five times the beam radius and beneath a depth that is five times the absorption length is very small and negligible, Eqs. (28) and (29) can be modified as Eqs. (30) and (31) respectively, without significant changes.

$$T'(X',Y',Z') = \int_{X_1'=-5}^{5}\int_{Y_1'=-\sqrt{25-X'^2}}^{\sqrt{25-X'^2}}\int_{Z_1'=-5}^{5}[f+(1-f)(X_1'^2+Y_1'^2)]\exp[-(X_1'^2+Y_1'^2)] \times \frac{\exp\left\{Pe\left[(X'-X_1')-\sqrt{(X'-X_1')^2+(Y'-Y_1')^2+(Z'-Z_1')^2}\right]-\frac{|Z_1'|}{\gamma'}\right\}}{\sqrt{(X'-X_1')^2+(Y'-Y_1')^2+(Z'-Z_1')^2}}\,dZ_1'\,dY_1'\,dX_1' \tag{30}$$

$$T'(X',Y',Z') = 2\gamma'\int_{X_1'=-5}^{5}\int_{Y_1'=-\sqrt{25-X'^2}}^{\sqrt{25-X'^2}}[f+(1-f)(X_1'^2+Y_1'^2)]\exp[-(X_1'^2+Y_1'^2)] \times \frac{\exp\left\{Pe\left[(X'-X_1')-\sqrt{(X'-X_1')^2+(Y'-Y_1')^2+(Z'-Z_1')^2}\right]\right\}}{\sqrt{(X'-X_1')^2+(Y'-Y_1')^2+(Z'-Z_1')^2}}\,dY_1'\,dX_1' \tag{31}$$

For thermal models based on Eqs. (30) and (31) as well as other structural modes of laser beams with definite heating domains, the Gauss–Legendre quadrature is appropriate for calculation of the thermal fields [25]. In order to deal with the singularities at the integration points, any interpolation function used in the finite element method can be used to describe the temperature distribution within the integration domain. In the present work, the linear interpolation was used. Fig. 3 shows the schematic relationship between the Gauss–Legendre points, $(X_1'^i, Y_1'^{ij}, Z_1'^k)$, $(i = 1,2,\ldots;\ j = 1,2,\ldots,\ k =$

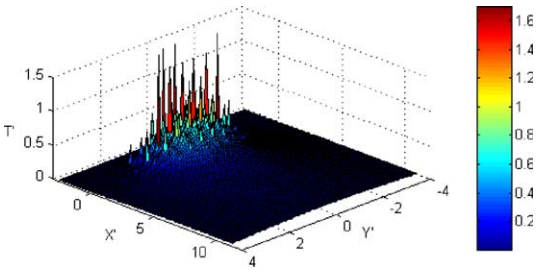

Fig. 2. A singular surface temperature distribution produced from Eq. (29) using numerical integration for $Pe = 1.47$, $\gamma' = 0.138$ and $f = 0.35$.

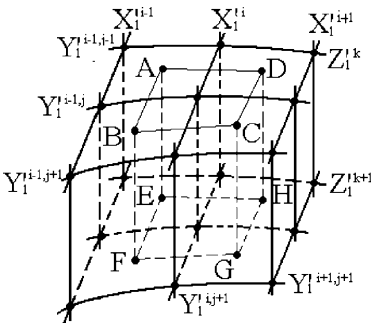

Fig. 3. A schematic relationship between the Gauss–Legendre points and the interpolation nodes used to describe the temperature distribution within the integration domain.

$1, 2, \ldots$), and the interpolation nodes in the case of the volumetric heating source. Each of the nodes chooses the central point of the four near-neighbour Gauss–Legendre points. Briefly, the temperature of any point within a hexahedron composed of eight near-neighbour nodes is expressed as a linear interpolation function of the eight nodes. In the case of a surface heating source, the integration domain is separated into corresponding quadrilaterals and the temperature is expressed as a linear interpolation function of four near-neighbour nodes. Good accuracy of the interpolation can be accomplished by applying sufficient integration points and correspondingly sufficient interpolation nodes. Further details on such a linear interpolation can be obtained from any literature on the finite element method, for instance, [23,26], and, hence, are not repeated here.

Although the integration domain is separated into discrete regions, as in the finite element method, the present model only needs to calculate the local temperatures of eight or four nodes simultaneously for calculation of the temperature at a point within the integration domain. If the point is outside the integration domain, it is not necessary to use the linear interpolation and the temperature can be directly calculated with the numerical integration. Thus, the present model can assure rapid calculation for the above-mentioned purpose of prediction.

With application of the linear interpolation to deal with the singularities associated with the numerical integration, the calculation procedure for prediction of the melt cross-sections is carried out according to the following steps:

(i) Calculate the dimensionless temperature distribution on the workpiece surface and, thus, find the maximum dimensionless temperature. According to Eq. (27), with respect to a set of laser beam radius and workpiece moving velocity, by taking P_V as zero, determine the minimum laser power required for the occurrence of melting and vaporization of the workpiece material from the maximum dimensionless temperature corresponding to the dimensionless melting point and boiling point, respectively.

(ii) For a set of laser process parameters, including the power, beam radius and workpiece moving velocity, if the power is between the minimum powers required for the occurrence of the melting and vaporization, then directly calculate the parameters of the melt cross-sections from step (iv). If the power is larger than the minimum power required for the occurrence of vaporization, take half the over power as the initial value of P_V and perform an iteration step (iii) to determine the heat loss due to vaporization, prior to step (iv).

(iii) According to the dimensionless boiling point defined in Eq. (27), find a contour of the vapour/melt interface on the workpiece surface according to the dimensionless temperature distribution obtained in step (i). Considering x and y within the contour, determine the profile of the cross-section of the vapour/melt interface, $z_{vpcs}(y)$, with a maximizing algorithm based on a seventh polynomial of x for a given value of y. Successively calculate a new heat loss due to vaporization according to Eqs. (23) and (26). Repeat this step until convergence of the heat loss reaches a limiting value.

(iv) Determine the cross-sectional profile of the melt/solid using a method similar to that in step (iii), although the dimensionless boiling point and vapour/melt interface are replaced by the dimensionless melting point and melt/solid interface, respectively, no iteration process is needed. Finally calculate the melt depth, half-width and cross-section area according to Eqs. (18)–(20).

3. Experimental procedure

The high-volume alumina-based refractory used to validate the present model was the same as that investigated in [4,5,20,21]. Table 1 lists the related physical properties of the material needed for the model. For the purpose of experimental convenience, the as-received refractory brick was sectioned into squares of $100 \times 50 \times 20$ mm^3 prior to laser surface melting.

Table 1
The physical properties of the high-volume alumina-based refractory used for the modeling

Property	Value	Reference
ρ (kg/m^3)	3180	[5]
K (W m^{-1} K^{-1})	3.25	[4]
$\alpha\times10^{-6}$ (m^2/s)	0.85	[4,5]
γ (μm)	345	[20,21]
R	0.15	[5]
T_m (K)	2373	[5]
T_b (K)	3223	[4,27,28]
L_V (kJ/kg)	4102	[4,27,28]

The laser used was a CO_2 laser (Rofin-Sinar) emitting at 10.6 μm and operating in the continuous wave (CW) mode with a maximum output power of 1.2 kW. The CO_2 laser beam was delivered to the workpiece surface by focusing the beam through a 150 mm focal length ZnSe lens. The laser optics were protected by means of a coaxially-blown Ar shield gas jet at a rate of 5 l/min. The workpieces were driven by an x–y CNC table. Various laser processing values for the laser power, beam size and workpiece moving velocity were used for the parametric investigation, as listed in Table 2.

The cross-sectional profiles of the melt/solid interfaces were measured using an image analysis method. The measurements involved the following steps: (a) observe the original images of the melt cross-sections using an optical microscope (OM), (b) obtain the grey level images of 768×512 pixel using a CCD camera, (c) produce binary images from the grey level images and find the edges of the melt/solid interface by specifying suitable thresholds. The last step was accomplished using the image analysis toolbox of the MATLAB R12 software (The Mathworks, Inc.). A representative grey level image and the corresponding cross-sectional profile of the melt/solid interface are illustrated in Fig. 4. Note that some spherical pores were present along the melt edge and their shapes were distinguished from those in the untreated refractory brick. Thus, these spherical pores should be included in the melt cross-section. For

Table 2
Comparison of experimental and predicted melt depths, half-widths and cross-section areas

Laser processing parameter			Experimental results			Prediction from surface source			Prediction from volumetric source		
P (W)	d (mm)	U (mm/s)	W_E (mm)	D_E (mm)	S_E (mm^2)	W_S (mm)	D_S (mm)	S_S (mm^2)	W_V (mm)	D_V (mm)	S_V (mm^2)
500	10	1	3.56 (0.11)	1.68 (0.04)	7.50 (0.20)	3.81	2.11	10.77	3.64	1.96	10.66
600	10	1	3.70 (0.20)	2.05 (0.11)	9.80 (0.80)	4.16	2.40	13.87	4.00	2.30	13.66
700	10	1	3.86 (0.06)	2.22 (0.12)	11.65 (0.81)	4.41	2.67	16.88	4.28	2.61	16.58
800	10	1	3.90 (0.05)	2.83 (0.03)	15.25 (0.45)	4.61	2.93	19.84	4.50	2.90	19.47
900	10	1	4.25 (0.09)	2.97 (0.16)	16.94 (1.09)	4.82	3.18	22.87	4.70	3.17	22.33
1000	10	1	4.74 (0.21)	3.40 (0.09)	19.94 (0.74)	5.00	3.42	25.83	4.90	3.43	25.29
1000	10	3	3.47 (0.21)	1.63 (0.02)	8.03 (0.54)	3.74	1.68	9.02	3.52	1.66	8.87
1000	10	5	3.09 (0.09)	0.99 (0.13)	4.38 (0.31)	3.27	1.16	5.34	3.01	1.14	5.28
1000	10	7	2.92 (0.09)	0.86 (0.06)	3.30 (0.16)	2.99	0.90	3.73	2.69	0.87	3.70
1000	10	9	2.60 (0.03)	0.56 (0.01)	2.15 (0.05)	2.77	0.74	2.83	2.40	0.68	2.57
600	8	7	1.97 (0.10)	0.60 (0.05)	1.73 (0.10)	2.22	0.71	2.14	1.82	0.61	1.71
700	10	5	2.56 (0.03)	0.79 (0.01)	2.58 (0.08)	2.78	0.92	3.28	2.48	0.82	3.10
800	6	3	2.56 (0.03)	1.81 (0.03)	6.41 (0.15)	2.79	1.75	7.35	2.64	1.78	7.19
900	12	1	4.83 (0.05)	2.82 (0.03)	16.99 (0.34)	5.17	3.02	22.33	5.03	2.94	21.89

Note that the experimental data in parentheses stand for the differences of lower or upper bounds from the average values.

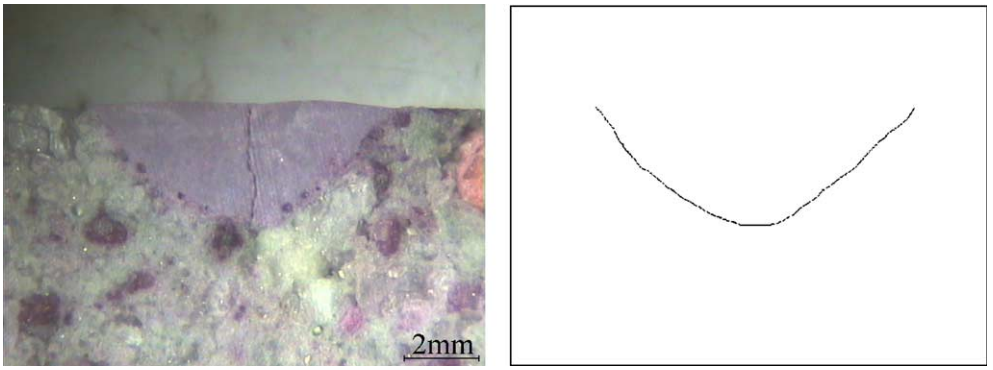

Fig. 4. A representative OM grey level image and the corresponding cross-sectional profile of the melt/solid interface for $P = 1000$ W, $d = 10$ mm and $U = 1.0$ mm/s. Note the vertical crack formed due to thermal-induced stress.

each sample, three measurements were repeated to obtain the average values for melt width, depth and cross-section area.

4. Results and discussion

This section includes the temperature distributions calculated from the present models, the minimum laser powers required for the occurrence of melting and vaporization, the melt depths and widths, the cross-sectional profiles of the melt/solid interfaces as well as the experimental evaluation. All calculations were executed using the MATLAB R12 (The Mathworks, Inc.) on a PC computer with GenuineIntel x86 Family 6 Model 8 Stepping 10 processor and 255.0 MB RAM. The calculations were based on the material properties listed in Table 1 and confined to the laser process parameters of power from 100 to 1000 W, beam diameter from 6 to 12 mm and workpiece moving velocity from 1.0 to 9.0 mm/s. A fraction of the Gaussian mode $f = 0.35$ in Eqs. (21) and (22) was chosen for approximating the experimental CO_2 laser as shown in Fig. 5. Except for the data used to compare the experimental results, the other data points drawn in the following figures were calculated using the process parameters of the complete combination of the laser power ranked into 10, beam diameter into four and workpiece moving velocity into five equal levels.

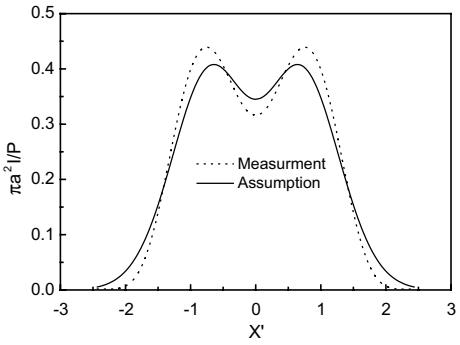

Fig. 5. Comparison of the assumed and the measured laser intensity profiles.

4.1. Temperature distribution

Fig. 6 presents the dimensionless temperature contours on the surface of the workpiece for $Pe = 1.47$ calculated from the two models using a volumetric heating source and a surface heating source, respectively. See Eq. (27) for the definition of Pe. The singularities associated with the numerical integration have been completely avoided and the temperature distributions were smooth. Due to the motion of the workpiece in the positive x direction relative to the laser beam, which caused advection heat flow to occur in the same direction, the peak temperatures at the workpiece surface were near the trailing edge of the laser beam rather than at the beam centre.

Figs. 7 and 8 show the dimensionless temperatures calculated from the two models for different Péclet numbers as functions of X' at the X' axis and as functions of Z' at the line of $X' = 1.0$ and $Y' = 0$, respectively. It has been demonstrated that the temperature varies with the Péclet number for the surface heating source [17]. The present modeling is mainly concerned with the difference between the two heating sources. Near the workpiece surface, the temperatures calculated from the model using the volumetric heating source are lower than those calculated using the surface heating source for the various Péclet numbers. Away from the surface, for smaller Péclet numbers, the temperatures calculated from the models using the two heating sources are almost identical; however, for larger Péclet numbers, the temperatures calculated from the model using the volumetric heating source appear higher than those calculated using the surface heating source. This

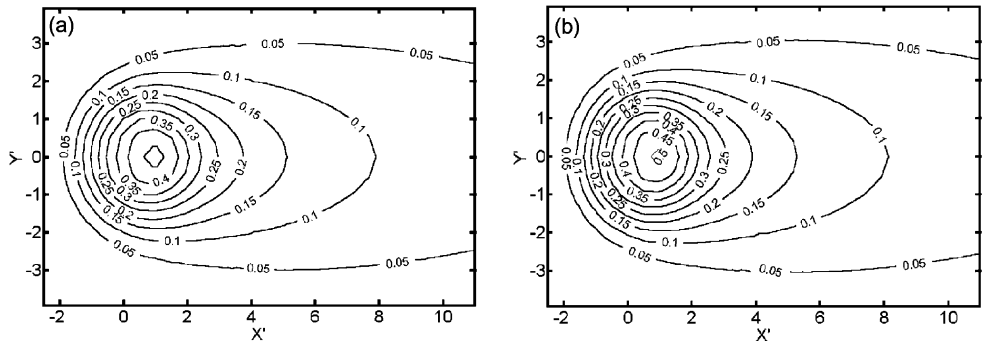

Fig. 6. The dimensionless temperature contours on the surface of the workpiece for $Pe = 1.47$, calculated from the two models using (a) the volumetric heating source and (b) the surface heating source, respectively.

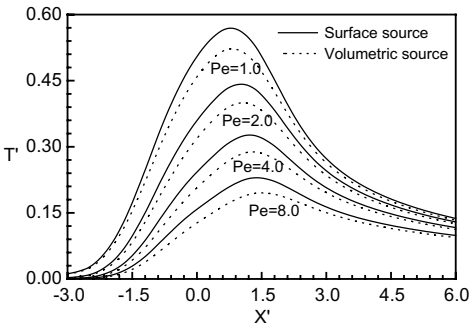

Fig. 7. The dimensionless temperatures calculated from the two models as functions of X' for various Péclet numbers at X' axis ($Y' = 0$, $Z' = 0$).

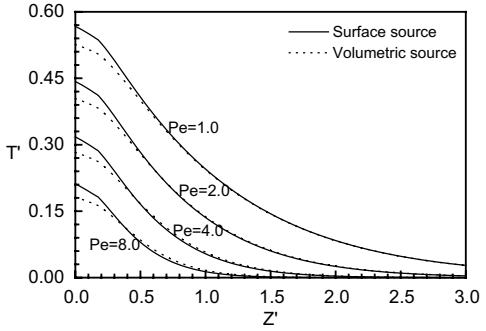

Fig. 8. The dimensionless temperatures calculated from the two models as functions of Z' for various Péclet numbers at the line of $X' = 1.0$ and $Y' = 0$.

result may be due to the fact that more heat absorbed by the workpiece surface can diffuse into the workpiece for a smaller Péclet number than for a larger Péclet number.

4.2. Minimum laser powers required for the occurrence of melting and vaporization

It is of practical importance to know the minimum laser powers required for the occurrence of melting and vaporization under different laser beam sizes and workpiece moving velocities. Fig. 9 gives the contour plots for the minimum laser powers from the two models using the volumetric heating source and the surface heating source required for the occurrence of melting as a function of workpiece moving velocity and laser beam diameter. In agreement with the peak temperatures dependent on the heating source shown in Fig. 7, the minimum laser power predicted using the volumetric heating source is clearly higher than that predicted using the surface heating source for an identical laser beam size and workpiece moving velocity.

Accordingly, it is also apparent from Fig. 7 that the minimum laser power predicted using the volumetric heating source required for the occurrence of vaporization is higher than that predicted using the surface heating source (Fig. 10). Previous investigations by Triantafyllidis et al. [5] indicated that a power of 680 W was appropriate for the refractory to be sealed, with the formation of a crack-free and pore-free surface using a beam of 12 mm diameter and a workpiece moving velocity of 0.4 mm/s. From Fig. 10, it can be seen that this power is much higher than the minimum laser powers of the two heating models required for the occurrence of vaporization. Thus, for development of an exact thermal model to analyze the laser surface melting of the refractory, the heat loss due to vaporization should not be neglected.

4.3. Melt depths and widths

From Figs. 6 and 7, it is clear that the melt width predicted from the model incorporating the volumetric heat source would always be smaller than that predicted

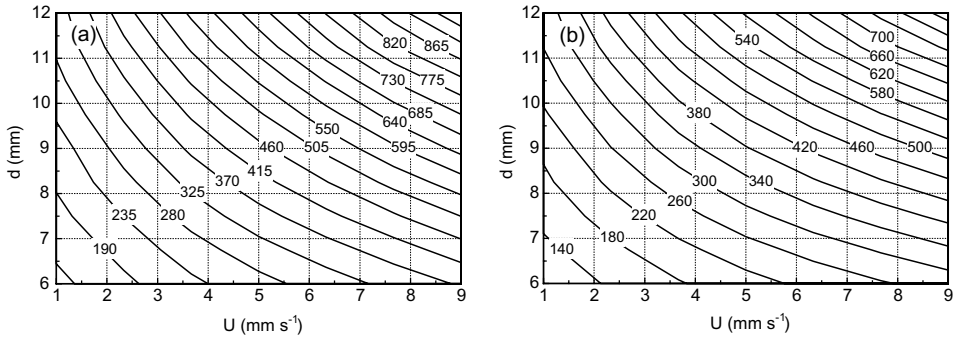

Fig. 9. The minimum laser powers (in Watt) for the two models using (a) the volumetric heating source and (b) the surface heating source required for the occurrence of melting as a function of workpiece moving velocity and laser beam diameter.

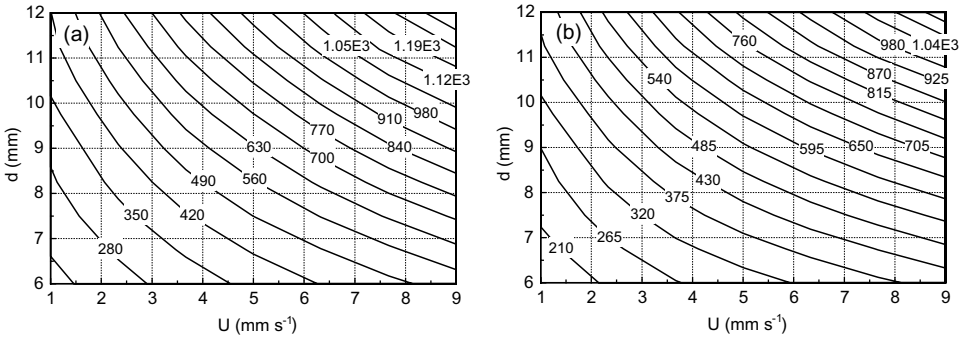

Fig. 10. The minimum laser powers (in Watt) for the two models using (a) the volumetric heating source and (b) the surface heating source required for the occurrence of vaporization as a function of workpiece moving velocity and laser beam diameter.

from the model incorporating the surface heating source, no matter what the laser process parameters. However, from Fig. 8, it is also clear that the melt depths predicted from the model using the volumetric heating source may be larger or smaller than those predicted from the model using the surface heating source.

Figs. 11 and 12 compare the relative errors in the melt depths and half-widths predicted from the model using the surface heating source with those predicted from the model using the volumetric heating source. Roughly, for the larger melt depths and half-widths, the values predicted from the two models were relatively close to each other. However, for smaller melt depths and widths (for example, less than 2.0 mm), considerable differences exist in the values predicted from the two models. This results from the fact that, for smaller melt depths and widths, a considerable amount of laser energy has been at once absorbed by material outside the melt pools for the model incorporating the volumetric heating source.

An analytic model derived by Lawrence et al. [18] showed a linear dependence of the melt depth in selected architectural materials on the ratio of $P/(\mathrm{d}U)^{1/2}$. Such a

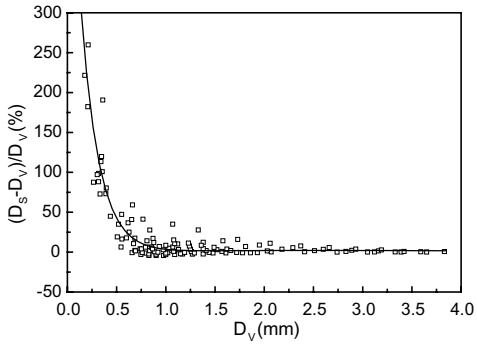

Fig. 11. The relative errors in the melt depths predicted from the model using the surface heating source to those predicted from the model using the volumetric heating source.

relationship was explored in the present modeling. Figs. 13 and 14 respectively show plots of the predicted melt depth versus $P/(\mathrm{d}U)^{1/2}$ and the predicted melt half-width versus $P/(\mathrm{d}U)^{1/2}$. It can be seen that, for both models, only within the local region of the laser process parameters, do approximately linear relationships occur

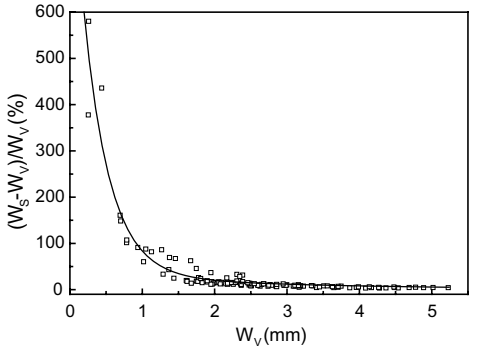

Fig. 12. The relative errors in the melt half-width predicted from the model using the surface heating source to those predicted from the model using the volumetric heating source.

between the predicted melt depth or half-width and $P/(\mathrm{d}U)^{1/2}$. This is reasonable because fewer assumptions were made in the present models than in the model given in [18].

4.4. Cross-sectional profiles of the melt/solid interfaces

Fig. 15 depicts plots of the melt cross-sectional area versus the product of the melt depth and half-width predicted from the two models using the volumetric heating source and the surface heating source respectively. The plot for the volumetric heating source showed excellent linearity, and that for the surface heating source also showed good linearity. Thus, the predicted cross-sectional profiles could be approximately described by the function defined by:

$$z_{\mathrm{cs}}(y)=\begin{cases} D\left[1-\left(\frac{|y|}{W}\right)^{\beta}\right] & |y|<W \\ 0 & |y|\geqslant W \end{cases} \tag{32}$$

and

$$S=\int_{y=-W}^{W} D\left[1-\left(\frac{|y|}{W}\right)\right]\mathrm{d}y=\frac{2\beta}{1+\beta}DW \tag{33}$$

The constant powers of β for the profiles predicted from the models using the volumetric heating source and

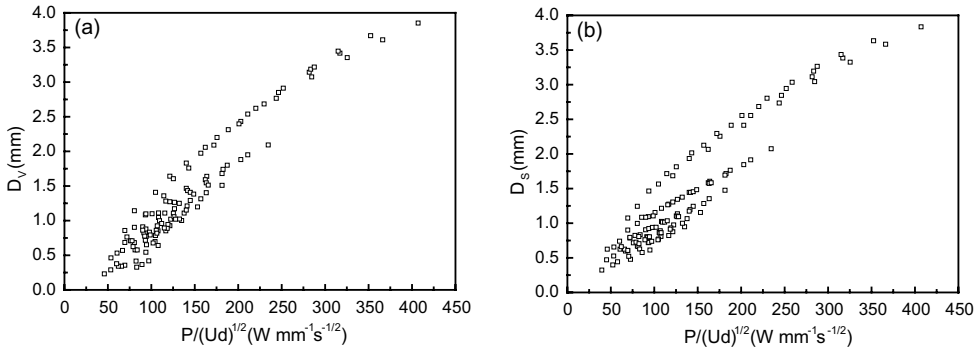

Fig. 13. Plots of the predicted melt depth, D, versus $P/(\mathrm{d}U)^{1/2}$ for the two models using (a) the volumetric heating source and (b) the surface heating source.

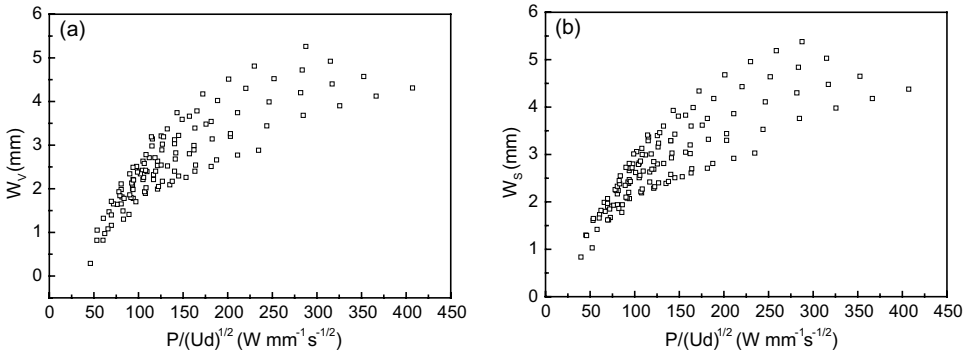

Fig. 14. Plots of the predicted melt half-width, W, versus $P/(\mathrm{d}U)^{1/2}$ for the two models using (a) the volumetric heating source and (b) the surface heating source.

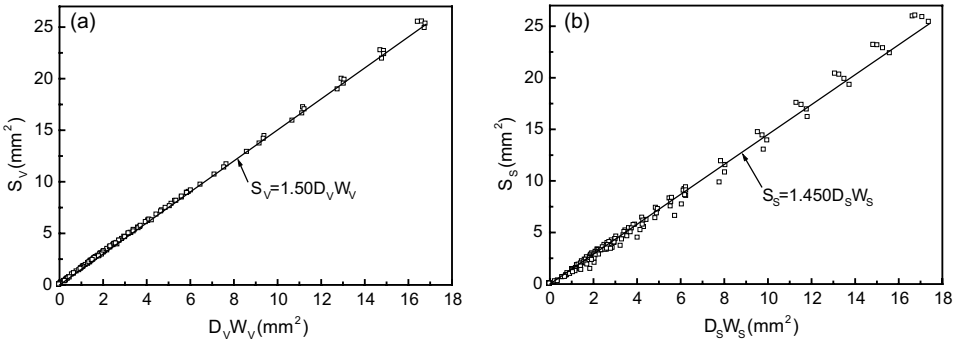

Fig. 15. Plots of the melt cross-section area, S, versus the product of the melt depth and half-width, DW, predicted from the two models using (a) the volumetric heating source and (b) the surface heating source.

the surface heating source were respectively 3.00 and 2.64.

4.5. Experimental evaluation

The accuracy of the melt cross-sectional parameters predicted from the models is evaluated by comparison with experimental results. The chosen laser process parameters, experimental and predicted melt depths, widths and cross-sectional areas are listed in Table 2. For the purpose of clarity, Figs. 16–18 show the predicted values as functions of the experimental results. Note that the straight lines in these figures represent the situation where the y-coordinate is equal to the x-coordinate. From these figures, it is evident that the model incorporating the volumetric heating source was more accurate than that incorporating the surface heating source for prediction of the melt depths, half-widths and cross-sectional areas. The melt depths and half-widths

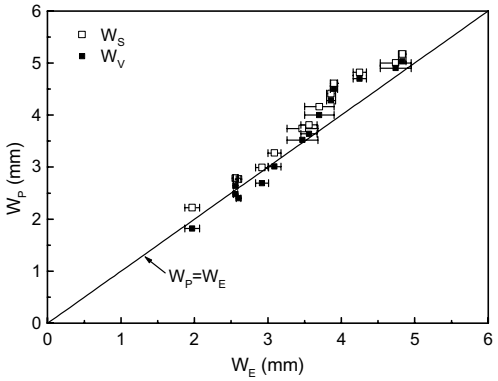

Fig. 17. Plots of the predicted melt half-width, W_P, versus experimental melt half-width, W_E, for the two models incorporating the volumetric heating source (solid squares) and the surface heating source (open squares). Note that the error bars stand for the lower and upper bounds of the measured data.

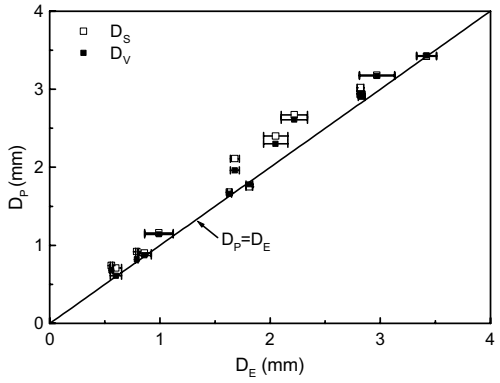

Fig. 16. Plots of the predicted melt depth, D_P, versus experimental melt depth, D_E, for the two models incorporating the volumetric heating source (solid squares) and the surface heating source (open squares). Note that the error bars stand for the lower and upper bounds of the measured data.

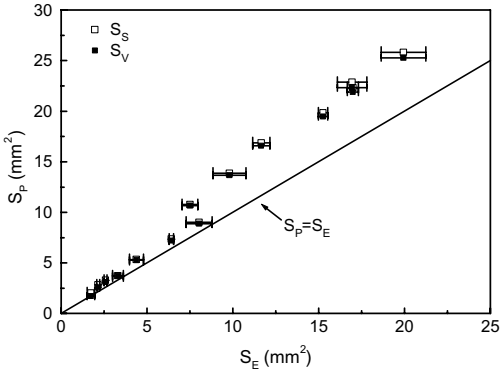

Fig. 18. Plots of the predicted melt cross-section area, S_P, versus experimental melt cross-section area, S_E, for the two models incorporating the volumetric heating source (solid squares) and the surface heating source (open squares). Note that the error bars stand for the lower and upper bounds of the measured data.

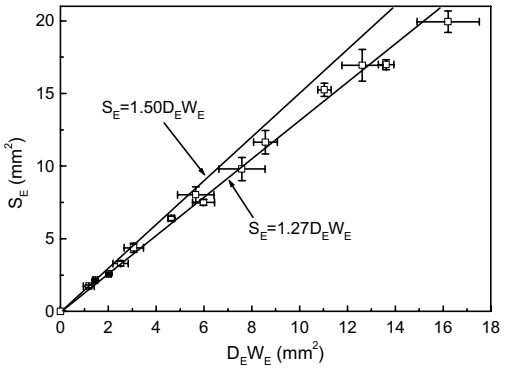

Fig. 19. Plot of the experimental melt cross-section area, S_E, versus the product of the melt depth and half-width, $D_E W_E$. Note that the error bars stand for the lower and upper bounds of the measured data.

predicted from the model incorporating the volumetric heating source were in good agreement with the experimental results. The predicted cross-sectional areas were also relatively consistent with the experimental data for smaller melt cross-sections. However, an increasing discrepancy is observed with increase in size of the melt cross-sections.

Fig. 19 shows a plot of the experimental melt cross-sectional area versus the product of the melt depth and the half-width. For small melt cross-sectional areas, for example less than 5 mm^2, a power of β close to 3.0, predicted from the model using the volumetric heating source, was acceptable for describing the cross-sectional profile from Eq. (32). However, in the outline, a smaller β value of 1.74 was obtained from Eq. (33). Fig. 20 further compares the melt cross-sectional profiles predicted from the two models with those measured using an image analysis method for two sets of laser process parameters. For the smaller melt cross-section, the profile predicted from the model using the volumetric heating source agreed very well with the measured profile; however, that predicted from the model using the surface heating source was obviously larger than that measured. For the larger melt cross-section, the profiles predicted from the two models were almost identical. The melt depths and widths predicted from the two models were relatively close to the measured values. However, the predicted profiles were somewhat fatter than the measured profile.

In addition to neglecting latent heat of fusion, the assumptions of a semi-infinite workpiece and temperature-independent properties, as well as the simplification of heat loss due to vaporization in the present modeling influenced the thermal fields. The above observed difference between small and larger melt pools can be more reasonably associated with the neglect of fluid flow within the melt pools. The flow within a melt pool is determined by the temperature-dependent surface tension and thermal buoyancy [8]. The energy equation including fluid flow is given by

$$\frac{\partial}{\partial x}(uT)+\frac{\partial}{\partial y}(vT)+\frac{\partial}{\partial z}(wT) = \alpha\nabla^2 T + U\frac{\partial T}{\partial x}+\frac{(1-R)q(x,y,z)}{\rho c} \tag{34}$$

From the balance between shear force and surface tension at the top surface of melt pool, it can be given

$$\tau_{xz} = -v\left(\frac{\partial u}{\partial z}\right)_{\text{top}} = \sigma_{\text{T}}\left(\frac{\partial T}{\partial x}\right)_{\text{top}} \tag{35a}$$

$$\tau_{yz} = -v\left(\frac{\partial v}{\partial z}\right)_{\text{top}} = \sigma_{\text{T}}\left(\frac{\partial T}{\partial y}\right)_{\text{top}} \tag{35b}$$

Following the work of Chakraborty et al. [29], Eqs. (34) and (35) can be scaled as

$$\frac{u_{\text{ref}}}{x_{\text{ref}}}+\frac{v_{\text{ref}}}{y_{\text{ref}}}+\frac{w_{\text{ref}}}{z_{\text{ref}}}+\alpha\left(\frac{1}{x_{\text{ref}}^2}+\frac{1}{y_{\text{ref}}^2}+\frac{1}{z_{\text{ref}}^2}\right) + \frac{U}{x_{\text{ref}}} \approx \frac{(1-R)q}{\rho c(T_{\max}-Tm)} \tag{36}$$

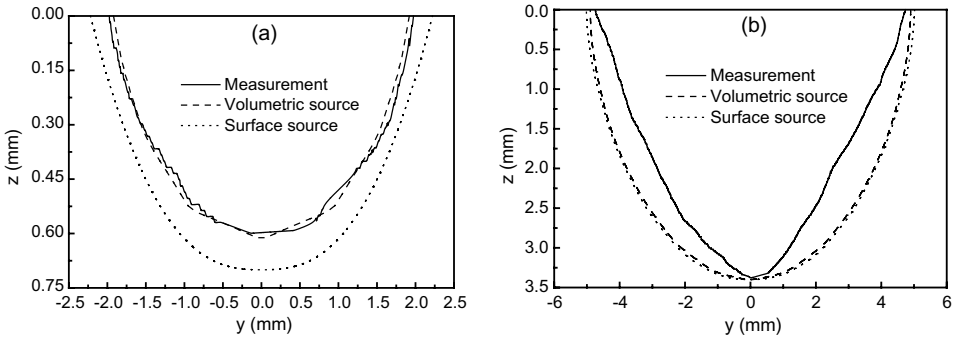

Fig. 20. The melt cross-section profiles predicted from the two models compared with those measured using image analysis method for (a) $P = 600$ W, $d = 8.0$ mm, $U = 7.0$ mm/s and (b) $P = 1000$ W, $d = 10.0$ mm, $U = 1.0$ mm/s.

$$v\frac{u_{\mathrm{ref}}}{z_{\mathrm{ref}}} \approx \sigma_{\mathrm{T}}\frac{T_{\max}-T_{\mathrm{m}}}{x_{\mathrm{ref}}} \tag{37a}$$

$$v\frac{v_{\mathrm{ref}}}{z_{\mathrm{ref}}} \approx \sigma_{\mathrm{T}}\frac{T_{\max}-T_{\mathrm{m}}}{y_{\mathrm{ref}}} \tag{37b}$$

Experimental results in Table 2 indicated that melt half-width and melt depth were of the same of order as laser beam radius. Thus, it is reasonable to use $x_{\mathrm{ref}} \approx y_{\mathrm{ref}} \approx z_{\mathrm{ref}} \approx a$ for a scaling analysis. Also, assume that the x, y and z components of reference velocity are of the same order as each other, and are all taken as u_{ref}. Then combing Eqs. (36) and (37), the following relation can be derived

$$\frac{3}{a}u_{\mathrm{ref}} + \frac{3\alpha}{a^2} + \frac{U}{a} \approx \frac{(1-R)\sigma_{\mathrm{T}}q}{\rho c v u_{\mathrm{ref}}} \tag{38}$$

From Eq. (38), one can obtain

$$u_{\mathrm{ref}} \approx \frac{\sqrt{(3\alpha+aU)^2 + \frac{12(1-R)a^2\sigma_{\mathrm{T}}q}{\rho c v}} - (3\alpha+aU)}{6a}. \tag{39}$$

For a given u_{ref}, the three terms in the left side of Eq. (38) can represent the relative ratios of laser energy consumed by fluid flow, thermal diffusion and workpiece moving. From Eqs. (38) and (39), it can be seen that the higher the effective heat flux, the larger the ratio of energy consumed by fluid flow. Therefore, for a smaller melt pool, the effect of fluid flow on the thermal field is negligible. For a larger melt pool, a considerable amount of energy is consumed by the fluid flow, which would lead to a decrease in the size of the melt pool to some extent. At the bottom centre and surface edge of the melt pool, there exist zones with zero velocity. The changes in the melt depth and width due to the flow are, hence, insignificant. Such fluid flow within the melt pool tends to result in leaner melt cross-sectional profiles [30]. Therefore, the models presently developed were able to provide a good understanding of some of the physical processes taking place during laser surface melting of ceramic materials. The model using the volumetric heating source was able to predict quite well the melt depths and widths. For larger melt pools, fluid flow should be included in future models used to determine the thermal and stress fields.

5. Conclusions

A thermal model incorporating a volumetric heating source for the prediction of melt cross-sections of ceramic material during laser surface melting has been developed and compared with a corresponding model incorporating a surface heating source. By applying a linear interpolation within the heating domain, the calculated temperature distributions were very smooth, without singularities.

The melt cross-sectional profiles predicted from the models using the volumetric heating source and the surface heating source respectively could be approximately described as a function of the melt depth and half-width.

Roughly, for melt depths and half-widths greater than 2.0 mm, the values predicted from the two models were relatively close to each other. However, for the melt depths and widths less than 2.0 mm, considerable differences existed between the values predicted from the two models.

From comparison with experimental results for a high-volume alumina-based refractory, the model incorporating the volumetric heating source was more accurate than that incorporating the surface heating source for prediction of melt depths, half-widths and cross-sectional areas. The melt depths and half-widths predicted from the model incorporating the volumetric heating source were in good agreement with the experimental results. The predicted cross-sectional areas were also reasonably consistent with the experimental data for smaller melt cross-sections. However, an increasing discrepancy was observed with increase in the size of the melt cross-sections, which was associated with the nature of fluid flow within the melt pool.

References

[1] J. Lawrence, L. Li, J.T. Spencer, The effects of high-power diode laser radiation on the wettability, adhesion and bonding characteristics of an alumina/silica-based oxide and vitreous enamel, Surf. Coat. Technol. 115 (1999) 273–281.

[2] J. Lawrence, E.P. Johnston, L. Li, Determination of absorption length of CO_2 and high-power diode laser radiation for ordinary Portland cement, J. Phys., D: Appl. Phys. 33 (2000) 945–947.

[3] M.J.J. Schmidt, L. Li, High power diode laser surface treatment of mullite crucible materials, Appl. Surf. Sci. 168 (2000) 9–12.

[4] L. Bradley, L. Li, F.H. Stott, Flame-assisted laser surface treatment of refractory materials for crack-free densification, Mater. Sci. Eng. A278 (2000) 204–212.

[5] D. Triantafyllidis, L. Li, F.H. Stott, Surface treatment of alumina-based ceramics using combined laser sources, Appl. Surf. Sci. 186 (2002) 140–144.

[6] Z. Liu, Crack-free surface sealing of plasma sprayed ceramic coatings using an excimer laser, Appl. Surf. Sci. 186 (2002) 135–139.

[7] A. Petitbon, D. Guignot, U. Fischer, J.M. Guillemot, Laser surface treatment of ceramic coatings, Mater. Sci. Eng., A: Struct. Mater.: Propert., Microstruct. Process. A 120–121 (1989) 545–548.

[8] L.X. Yang, X.F. Peng, B.X. Wang, Numerical modeling and experimental investigation on the characteristics of moltem pool during laser processing, Int. J. Heat Mass Transfer 44 (2001) 4465–4473.

[9] M. Leung, Phase-change heat transfer in laser transformation hardening by moving Gaussian rectangular heat source, J. Phys., D: Appl. Phys. 34 (2001) 3434–3441.
[10] Y. Zhang, A. Faghri, Vaporization, melting and heat conduction in the laser drilling process, Int. J. Heat Mass Transfer 42 (1999) 1775–1790.
[11] M. Davis, P. Kapadia, J. Dowden, W.M. Steen, C.H.G. Courtney, Heat hardening of metal surfaces with a scanning laser, J. Phys., D: Appl. Phys. 19 (1986) 1981–1997.
[12] J.M. Dowden, The Mathematics of Thermal Modeling, Chapman & Hall/CRC, Boca Raton, London, New York, Washington, DC, 2001, pp. 77–112.
[13] H.S. Carslaw, J.C. Jaeger, Conduction of Heat in Solids, Oxford University Press, London, 1959, pp. 265–268.
[14] H.E. Cline, T.R. Anthony, Heat treating and melting material with a scanning laser or electron beam, J. Appl. Phys. 48 (1977) 3895–3900.
[15] M. Lax, Temperature rise induced by a laser beam, J. Appl. Phys. 48 (1977) 3919–3924.
[16] M.F. Modest, H. Abakians, Heat conduction in a moving semi-infinite solid subjected to pulsed laser irradiation, J. Heat Transfer 108 (1986) 597–601.
[17] J. Cheng, A. Kar, Mathematical model for laser densification of ceramic coating, J. Mater. Sci. 32 (1997) 6269–6278.
[18] J. Lawrence, A.A. Peligard, E. Zhou, L. Li, D. Morton, Prediction of melt depth in selected architectural materials during high-power diode laser treatment, Opt. Lasers Eng. 35 (2001) 51–62.
[19] L.G. Hector, R.B. Hetnarski, Thermal stresses in materials due to laser heating, in: R.B. Hetnarski (Ed.), Thermal Stresses IV, Elsevier, Amsterdam, Lausanne, New York, Oxford, Shannon, Tokyo, 1996, pp. 453–531.
[20] J. Lawrence, L. Li, Determination of the absorption length of CO_2 and high power diode laser radiation for a high volume alumina-based refractory material, Appl. Surf. Sci. 168 (2000) 71–74.
[21] J. Lawrence, K. Minami, L. Li, R.E. Edwards, A.W. Gale, Determination of the absorption length of CO_2, Nd:YAG and high power diode laser radiation for a selected grouting material, Appl. Surf. Sci. 186 (2002) 162–165.
[22] Y. Zhang, A. Faghri, Thermal modeling of selective area laser deposition of titanium nitride on a finite slab with stationary and moving laser beams, Int. J. Heat Mass Transfer 43 (2000) 3835–3846.
[23] J.N. Reddy, D.K. Gartling, The Finite Element Method in Heat Transfer and Fluid Dynamics, CRC Press, Boca Raton, Ann Arbor, London, Tokyo, 1994, pp. 34–37.
[24] S. Chakraborty, P. Dutta, A generalized formulation for evaluation of latent heat functions in enthalpy-based macroscopic models for convection-diffusion phase change process, Metall. Mater. Trans. B 32B (2001) 562–564.
[25] M. Abramowitz, I.R. Stegun, Handbook of Mathematical Function with Formulas, Graphs, and Mathematical Tables, John Wiley & Sons, New York, Chichester, Brisbane, Toronto, Singapore, 1972, pp. 875–924.
[26] R.W. Lewis, K. Morgan, H.R. Thomas, K.N. Seetharamu, The Finite Element Method in Heat Transfer Analysis, John Wiley & Sons, Chichester, NewYork, Brisbane, Toronto, Singapore, 1996, pp. 17–32.
[27] D.R. Lide, H.P.R. Frederikse, CRC Handbook of Chemistry and Physics, CRC Press, Boca Raton, New York, London, Tokyo, 1995, pp. 4–34, 4–83.
[28] J.A. Dean, Lange's Handbook of Chemistry, 15th ed., McGraw-Hill, London, 1999, pp. 6–82, 6–112.
[29] S. Chakraborty, S. Sarkar, P. Dutta, A scaling analysis of momentum and heat transport in gas tungsten arc weld pools, Sci. Technol. Weld. Join. 7 (2) (2002) 88–94.
[30] J.F. Ready, LIA Handbook of Laser Materials Processing, Laser Institute of America, Orlando, Fla, 2001, pp. 265–268.